Vibration Analysis of a Nonlinear Absorber Coupled to a Hand-Held Impact Machine

Oreoluwa Alabi
Department of Biomedical Engineering and Mechanics,
Virginia Tech,
Blacksburg, VA 24061

Sunit Kumar Gupta
Department of Mechanical Engineering,
Virginia Tech,
Blacksburg, VA 24061

Oumar R. Barry[1]
Department of Mechanical Engineering,
Virginia Tech,
Blacksburg, VA 24061
e-mail: obarry@vt.edu

Exposure of human hands to harmful levels of vibration can lead to severe injuries. To attenuate these hand transmitted vibrations, a nonlinear vibration absorber inerter (NVAI) is proposed in this work. The proposed NVAI is attached to a coupled nonlinear system of a hand-held impact machine and a hand-arm system. The combined coupled nonlinear system is modeled as a lumped parameter model with a combination of cubic and linear stiffness components, linear viscous dampers, and lumped masses. The governing equations of motion are solved analytically using the method of harmonic balance and validated using numerical simulations. A numerical bifurcation diagram of the system reveals the existence of complex solutions such as quasi-periodic and chaotic attractors. The appearances of quasi-periodic and chaotic attractors are later confirmed by Lyapunov exponents. Further, we explore the ability of the proposed NVAI to decrease the area corresponding to unstable quasi-periodic and chaotic motion in the excitation amplitude–frequency space. This observation further implies the delay in the onset of quasi-periodic and chaotic motion for a range of forcing amplitude using Lyapunov exponents. Finally, parametric analyses are carried out to identify the critical design parameters of the NVAI. These analyses reveal that an increase in the damping, mass, and inertance of the absorber ameliorates the performance of the NVAI. Furthermore, the critical value of the external excitation, corresponding to a sudden change in the response of the system, can be controlled using an appropriate selection of absorber parameters. [DOI: 10.1115/1.4056803]

Keywords: method of harmonic balance, stability analysis, Floquet theory, Lyapunov exponents, bifurcation diagrams, phase portraits, Poincare maps

1 Introduction

Hand transmitted vibrations (HTVs) can be classified as the vibrations transmitted to the human hand-arm system through the handle of vibrating equipment. Severe exposure of the human hand to HTVs from hand-held impact machines (HIMs) puts humans at risk of developing hand-arm vibration syndrome (HAVS). HAVS is used to describe vascular, musculoskeletal, and neurological disorders [1–4]. Some of the symptoms of the neurological disorder include numbness and decreased tactile perception of the fingers. At the same time, the vascular disorders of HAVS may appear as frequent occurrences of finger blanching. These occurrences, also known as vibration white fingers [5], cause numbness, and pain in the hand. In extreme cases, vibration white finger can lead to permanent disability in humans. Therefore, it is required to understand the dynamics of the combined system of the human hand and HIMs for the better attenuation of HTVs. This is the focus of this work.

One of the popular methods to control undesired vibrations in different engineering structures is using a tuned vibration absorber (TVA) [6–8]. A traditional TVA consists of a mass-spring system tuned to the resonant frequency of a primary system [9]. Due to its simpler design, cost-effectiveness, and ease of installation, the use of TVAs is well-established in different applications such as grass trimmers, prismatic structures, overhead power lines, and regenerative chatter [10–16].

However, even though a TVA offers significant vibration reduction in a primary structure, it also suffers from a lack of robustness in the design as a slight variation in the tuned frequency will lead to the amplification of vibration instead of attenuation. This shortcoming in the TVA design can be overcome by including a nonlinear stiffness element in the design and making it a nonlinear TVA (NLTVA). Using a nonlinear stiffness element in the design of a TVA increases the effective bandwidth of the device's operating frequency, thus making it more applicable than a linear TVA [17–21]. In the next step toward the optimal design of the NLTVA, Habib et al. developed a tuning method for a nonlinear vibration absorber [22]. Furthermore, they observed that vibration absorbers are more effective when they exhibit the same restoring force characteristic as the primary systems. This observation further implies that it is essential to understand the underlying nonlinearities inherent in an engineering structure for the optimum design of the corresponding vibration absorber.

Another strategy to enhance the performance of a vibration absorber is by increasing the mass of the absorber. As reported in the literature, a larger mass can enhance the absorber's performance by widening its vibration suppression bandwidth and reducing the peak vibration response [23–26]. However, an increase in the absorber's mass also causes an increase in the overall mass of the combined system of the primary system and vibration absorber and is not feasible for many engineering applications due to design limitations. In order to avoid this tradeoff, mass amplification devices called inerters have been coupled to vibration absorbers. Inerters are two-terminal devices that produce a force proportional to the relative acceleration of their terminals [27]. The mass-boosting effects of inerters are highlighted by realizing a 300 kg effective mass from a 2 kg inerter [28]. It has been shown that the addition of an inerter in the design of an NLTVA provides better vibration control over a linear TVA and NLTVA without an inerter [25]. This observation further implies that it is beneficial to add a more inerter in the design of an NLTVA for better performance, making it a nonlinear-tuned-vibration-absorber-inerter (NVAI).

[1]Corresponding author.

Manuscript received October 26, 2022; final manuscript received January 2, 2023; published online May 4, 2023. Assoc. Editor: Teresa Berruti.

We emphasize that although the use of an NLTVA with an inerter is well-established in the literature for vibration attenuation in various engineering applications, it has not been implemented for vibration mitigation in an HIM. To the author's best knowledge, Golysheva et al. [29] were the first ones to analyze the dynamics of an HIM with a linear TVA in combination with a vibration isolator. They observed that this vibration attenuation design is beneficial for vibration reduction in the HIM without adding any significant cost to the design. It should be noted that in the study mentioned above, a linear model of the HIM was considered for the analysis. However, in more realistic situations, the HIM exhibits nonlinearity due to the tool-structure interaction, friction between the contact surfaces, and loss of contact between the tool and material [30]. These nonlinearities can be included in the model using individual or a combination of time-delay, quadratic, and cubic terms [30–32]. In this work, for simplicity in the analysis, we consider a model of the HIM with cubic nonlinearity. Also, as mentioned earlier, a linear TVA lacks robustness in the design. Therefore, in this work, for the first time, we consider an NLTVA with an inerter for the vibration control in a nonlinear model of the HIM and hand-arm system. Preliminary nonlinear analysis of the system reveals that the NVAI is effective for better vibration suppression in the HIM [25]. However, in this work, a nonlinear analysis of the system using Lyapunov exponents and Poincare map reveals the existence of more complex solutions such as quasi-periodic and chaotic motions. A parametric analysis is also conducted in this work to identify the key design parameters of the NVAI. The rest of the paper is organized as follows. In Sec. 2, a brief description of the mathematical model of the NVAI coupled with the HIM and hand-arm system is presented along with the nondimensionalization of the model. In Sec. 3, an analytical nonlinear analysis of the system is presented using the method of harmonic balance, and the linear stability analysis of the system is also presented. A discussion of linear and nonlinear analysis, numerical bifurcation analysis, Lyapunov exponents, and phase methodology are presented in Sec. 4. A parametric analysis assessing the impact of the various absorber parameters on the system is presented in Sec. 5. Finally, some conclusions are drawn in Sec. 6.

2 The Mathematical Model of a Hand-Held Impact Machines-Hand-Arm System-Nonlinear Vibration Absorber Inerter System

In this section, we formulate a lumped parameter model to analyze the dynamics of a hand-arm system (HAS) coupled with an HIM and a NVAI. The schematic of the combined system is shown in Fig. 1. In the current analysis, we employ the HAS proposed by Dong et al. [33]. Also, nonlinearity is introduced in the lumped parameter model of the system by including nonlinearity in the HIM and NVAI, as shown in Fig. 1. For the sake of simplicity in the analysis, we consider the nonlinearity in the HIM as cubic. Due to nonlinearities exhibited in an impact tools operation, via friction between contact surfaces or loss of contact between tool and material, the nonlinearities in the HIM are modeled as cubic. Therefore, the nonlinearity of the NVAI should also be cubic for better vibration suppression [22]. In Fig. 1, m_H, m_s, m_a, and m_n represent the masses of the HIM, human-hand skin in contact with the handle of HIM, hand-arm system, and the absorber, respectively. k_H and k_{HL} represent the nonlinear and linear ground connection stiffness, respectively, whereas, k_N and k_{NL} represent the nonlinear and linear stiffness of the NVAI, respectively. c_H and c_N represent the linear viscous damping coefficient of the HIM and NVAI, respectively. Further, k_s and c_s are the linear spring and viscous elements connecting the masses m_a and m_s, respectively, while k_a and c_a are the linear spring and viscous elements connecting the mass m_a to the body/trunk (modeled as a fixed surface), respectively. The inertance, which is grounded on one side and coupled to the mass of the absorber on the other side, is represented by b.

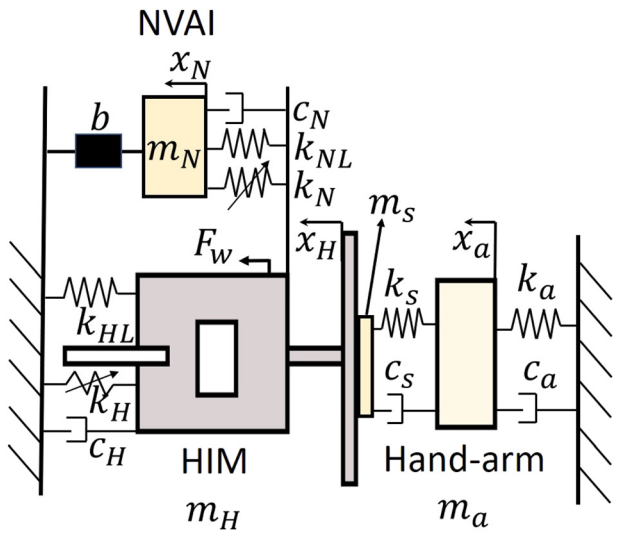

Fig. 1 Schematic of the combined system of HIM-HAS system with a NVAI

If x_H, x_a, and x_N represent the motion of HIM, HAS, and NVAI, respectively, then the governing equations of motion are given by

$$[\mathbf{M}]\{\ddot{\mathbf{x}}\} + [\mathbf{C}]\{\dot{\mathbf{x}}\} + [\mathbf{K}]\{\mathbf{x}\} + \{\mathbf{f_{nl}}\} = \{\mathbf{F_{eq}}\} \tag{1}$$

where $[\mathbf{M}]$, $[\mathbf{C}]$, and $[\mathbf{K}]$ are (4×4) inertia, damping, and stiffness matrices, respectively, $\{\mathbf{f_{nl}}\}$ represents the nonlinear force terms for the system, $\{\mathbf{F}_{\text{eq}}\}$ is a (3×1) force vector and $\{\mathbf{x}\} = [x_H, x_a, x_N]'$ is a (3×1) displacement coordinate vector. These matrices are defined in the Appendix.

In the above governing equations of motion, F_w represents the excitation force acting on the HIM due to the reciprocating motion of the piston inside the HIM. The analytical form of F_w is adapted from the experiments reported in Ref. [34] and is given by

$$F_w = F_{\text{ref}} \left(\frac{\omega}{\omega_{\text{ref}}} \right)^2 \sin(\omega t) \tag{2}$$

To reduce the effective number of parameters, we nondimensionalize the governing equations of motion, and accordingly, introduce the following scales and nondimensional parameters:

$$m_1 = m_H + m_s, \quad m_2 = m_N + b, \quad m_3 = m_a, \quad \omega_1 = \frac{k_{HL}}{m_1},$$

$$\tau = t\omega_1, \quad x_0 = \frac{g}{w_1^2}, \quad y = \frac{x}{x_0}, \quad \Omega = \frac{\omega}{\omega_1},$$

$$\zeta_1 = \frac{c_H}{2\sqrt{m_1 k_{HL}}}, \quad \zeta_2 = \frac{c_s}{2\sqrt{m_1 k_{HL}}}, \quad \zeta_3 = \frac{c_N}{2\sqrt{m_1 k_{HL}}}, \quad k_{r1} = \frac{k_s}{k_{HL}},$$

$$k_{r2} = \frac{k_{NL}}{k_{HL}}, \quad k_{rnl1} = \frac{k_H x_0^2}{k_{HL}}, \quad k_{rnl2} = \frac{k_N x_0^2}{k_{HL}}$$

$$F = \frac{F_{ref}}{m_1 x_0 \omega_{ref}^2}, \quad \alpha = \frac{m_1}{m_2}, \quad k_{r3} = \frac{k_a}{k_{HL}}, \quad \alpha_2 = \frac{m_1}{m_3},$$

$$\zeta_4 = \frac{c_a}{2\sqrt{m_1 k_{HL}}}$$

Using above mentioned scales and nondimensional parameters, Eq. (1) can be nondimensionalized as

$$[\mathbf{M1}]\{\mathbf{y}''\} + [\mathbf{C1}]\{\mathbf{y}'\} + [\mathbf{K1}]\{\mathbf{y}\} + \{\mathbf{f1_{nl}}\} = \{\mathbf{F1_{eq}}\} \tag{3}$$

where $[\mathbf{M1}], [\mathbf{C1}]$, and $[\mathbf{K1}]$ are (4×4) matrices with nondimensional parameters, $\{\mathbf{f1_{nl}}\}$ represents the nonlinear force terms for the system, $\{\mathbf{F1_{eq}}\}$ is a (3×1) force vector, and $\{\mathbf{y}\} = [y_H, y_N, y_a]'$ is a (3×1) displacement coordinate vector. These matrices are defined in the Appendix.

Prime $(')$ denotes the derivative with respect to the nondimensional time τ. For the analytical treatment of the coupled system, we rewrite Eq. (3) in a compact state-space form as

$$y_1' = y_2 \tag{4a}$$

$$y_2' = 2\zeta_1 y_2 - y_1 - 2\zeta_2(y_2 - y_4) - k_{r1}(y_1 - y_3) - k_{r2}(y_1 - y_5) - 2\zeta_3(y_2 - y_6) - k_{rnl1}y_1^3 - k_{rnl2}(y_1 - y_5)^3 + F\Omega^2\sin(\Omega\tau), \tag{4b}$$

$$y_3' = y_4 \tag{4c}$$

$$y_4' = -2\zeta_3\alpha(y_6 - y_2) - k_{r2}\alpha(y_5 - y_1) - k_{rnl2}\alpha(y_5 - y_1)^3 \tag{4d}$$

$$y_5' = y_6 \tag{4e}$$

$$y_6' = -k_{r3}\alpha_2 y_3 - 2\zeta_4\alpha_2 y_4 - k_{r1}\alpha_2(y_3 - y_1) - 2\zeta_2\alpha_2(y_4 - y_2) \tag{4f}$$

where $[y_1, y_2, y_3, y_4, y_5, y_6] = [y_H, y_H', y_N, y_N', y_a, y_a']$. Having established the nondimensional governing equations of motion, next we present the analytical solution procedure along with the linear stability analysis in Sec. 3.

3 Analytical Solution and Stability Analysis

The linear stability analysis of a nonlinear system is an important step and has to be performed carefully as it provides the critical values of the control parameters at which steady-states lose or gain stability. Note that the coupled nonlinear system in the current analysis, i.e., Eq. (4), is a nonautonomous system with a harmonic excitation; therefore, the steady-states will always be periodic in nature instead of being constants as in the case of an autonomous system. Since a linear stability analysis uses steady-state solutions, we first obtain the steady-state periodic solutions of the coupled nonlinear system using the method of harmonic balance, as presented next.

3.1 Analytical Solution Using the Method of Harmonic Balance. As mentioned earlier, we use the method of harmonic balance to get the steady-state periodic solutions of the current nonlinear system. Since linear methods are not sufficient to analyze systems expressing nonlinearity, the method of harmonic balance is employed to study the cubic nonlinearity embedded in our system. The method of harmonic balance works by representing a steady-state periodic solution of an ordinary or differential-algebraic equation system by a Fourier series, i.e., a combination of sinusoids [35]. The implementation of the method of harmonic balance for this system is presented below.

To proceed with the method of harmonic balance, we assume that the steady-state periodic solutions of Eq. (4) are synchronous with the external forcing on the system. The analysis of a duffing oscillator by Krack and Gross [35] revealed that a single harmonic term in the harmonic balance method could sufficiently capture the response of a forced duffing oscillator. Therefore, since our system contains the same form of nonlinearity, the solution of Eq. (4) can be assumed as

$$\{\mathbf{y}\}(\tau) = \{\mathbf{C}\}\cos(\Omega\tau) + \{\mathbf{D}\}\sin(\Omega\tau) \tag{5}$$

with coefficient vector $\mathbf{C}$ and $\mathbf{D}$ are defined as

$$\mathbf{C} = \begin{bmatrix} C_1 & C_2 & C_3 & C_4 & C_5 & C_6 \end{bmatrix}^T,$$
$$\mathbf{D} = \begin{bmatrix} D_1 & D_2 & D_3 & D_4 & D_5 & D_6 \end{bmatrix}^T$$

On substituting the assumed form of the solution in Eq. (4) we get

$$-\Omega\{\mathbf{C}\}\sin(\Omega t) + \Omega\{\mathbf{D}\}\cos(\Omega t) + \Omega[\mathbf{A}]\{\mathbf{C}\}\cos(\Omega t) + \Omega[\mathbf{A}][\mathbf{D}]\sin(\Omega t) + [\mathbf{N}_1] = \{\mathbf{F}_{eq}\} \tag{6}$$

where $[\mathbf{A}]$ is a (6×6) matrix and both $[\mathbf{N}_1]$ and $[\mathbf{F}_{eq}]$ are (6×1) column vectors. $[\mathbf{N}_1]$ contains the nonlinear terms of the equation. These matrices are defined in the Appendix.

By equating the coefficients of sine and cosine to zero in Eq. (6), we get the set of 12 simultaneous nonlinear algebraic equations in terms of coefficients of $\mathbf{C}$ and $\mathbf{D}$. These equations can be solved for $C_i s$ and $D_i s$, which further provide us the solution to nonlinear coupled system (Eq. (4)) by utilizing Eq. (5). Having obtained the steady-state solution to the nonlinear system, next, we present the linear stability analysis.

3.2 Linear Stability Analysis. To perform the linear stability analysis of steady-state periodic solutions, we provide a small perturbation to all steady-states as

$$y_i(\tau) = y_{is}(\tau) + \epsilon z_i(\tau), \quad \text{for} \quad i = 1, 2, 3, 4, 5, 6 \tag{7}$$

where $y_{is}s$ are the steady-state solutions of the system (obtained using the method of harmonic balance) and $\epsilon z_i s (\ll 1)$ represents small perturbations around the steady-states. Since the steady-state periodic solutions, i.e., $y_i(\tau)s$, of Eq. (4) satisfy Eq. (4), we get linearized equations in terms of perturbed and steady-state quantities as

$$z_1' = z_2 \tag{8a}$$

$$z_2' = -z_1 k_{r1} + z_3 k_{r1} - z_1 k_{r2} + z_5 k_{r2} - 3y_{1s}^2 z_1 k_{rnl1} - 3y_{1s}^2 z_1 k_{rn12} + 3y_{1s}^2 z_5 k_{rn12} + 6y_{5s}y_{1s}z_1 k_{rn12} - 6y_{5s}y_{1s}z_5 k_{rn2} - 3y_{5s}^2 z_1 k_{rn2} + 3y_{5s}^2 z_5 k_{rn2} + 2\zeta_1 z_2 - 2\zeta_2 z_2 + 2\zeta_2 z_4 - 2\zeta_3 z_2 + 2\zeta_3 z_6 - z_1 \tag{8b}$$

$$z_3' = z_4 \tag{8c}$$

$$z_4' = 3\alpha y_1^2 z_1 k_{rn2} - 3\alpha y_1^2 z_5 k_{rn12} - 6\alpha y_5 y_1 z_1 k_{rn2} + 6\alpha y_5 y_1 z_5 k_{rn2} + 3\alpha y_5^2 z_1 k_{rn2} - 3\alpha y_5^2 z_5 k_{rn2} + \alpha kr2 z_1 - \alpha kr2 z_5 + 2\alpha\zeta_3 z_2 - 2\alpha\zeta_3 z_6, \tag{8d}$$

$$z_5' = z_6 \tag{8e}$$

$$z_6' = \alpha_2 z_1 k_{r1} - \alpha_2 z_3 k_{r1} - \alpha_2 z_3 k_{r3} + 2\alpha_2\zeta_2 z_2 - 2\alpha_2\zeta_2 z_4 - 2\alpha_2\zeta_4 z_4 \tag{8f}$$

It should be noted here that the linearized equations, i.e., Eq. (8) involve time-periodic coefficients in terms of steady-states, so it is difficult to get the closed-form expressions for the critical values of the control parameters. Therefore, we use the Floquet theory to determine the stability of the steady-state periodic solutions numerically. A detailed discussion on linear stability along with nonlinear tools to explore the dynamics of the coupled system is presented in Sec. 4.

4 Results and Discussions

In this section, we first compare the analytical solution (Eq. (5)) with the numerical simulation of the coupled HIM-HAS-NVAI system to establish the accuracy of the analytical approach. The analytical solution presented earlier is used to generate a linear stability curve of the system in parametric space. Afterward, numerical bifurcation analyses of the system are used to examine

Table 1 Parameter values of the HIM-HAS-NVAI system used for simulations

Parameter	Value	Unit	Parameter	Value	Unit	Parameter	Value	Unit
m_H	1.7	kg	k_{HL}	3.0×10^5	N/m	c_H	50	Ns/m
m_a	1.55	kg	k_a	4279	N/m	c_a	76	Ns/m
m_s	0.049	kg	k_s	62804	N/m	c_s	192.90	Ns/m
m_N	$0.02m_H$	kg	k_{NL}	13280	N/m	c_N	9.3	Ns/m
F_{ref}	300	N	ω_{ref}	26.1	Hz	b	$0.04m_H$	kg
k_H	3.0×10^8	Ns/m^3	k_N	2.5×10^6	Ns/m^3	x_0	5.72×10^{-5}	–
w_1	414.12	—	α_2	1.12	—	ζ_4	0.052	—
α	17.15	—	ζ_1	0.034	—	ζ_2	0.13	—
k_{r1}	0.21	—	k_{r2}	0.052	—	ζ_3	0.0083	—
k_{rnl1}	3.27×10^{-6}	—	k_{rnl2}	1.90×10^{-8}	—	k_{r3}	0.014	—

the nonlinear dynamics of the system for the different values of the operating parameters, i.e., F and Ω. Finally, a parametric analysis is conducted to identify key design parameters of the system.

4.1 Validation of the Analytical Results From Method of Harmonic Balance. As mentioned earlier, the first part of this analysis involves the validation of the analytical results obtained using the harmonic balance method (HBM) (Eq. (5)) by comparing it against the direct numerical simulations of the coupled HIM-HAS-NVAI system (Eq. (4)). For this purpose, we compare the frequency-response curve of the primary system, i.e., HAS (y_a) obtained using HBM and numerically for the parameter values listed in Table 1. The mass of the HIM is chosen to represent the mass of a typical pneumatic chipping hammer, and the other parameters of the Kelvin–Voigt model for the ground-stiffness interaction are chosen to represent parameters of a material acted on by a tool-bit. Furthermore, the linear and nonlinear parameters of the NVAI are determined by the H_∞ optimization method [36] and the principle of similarity [25,37], respectively.

Since it is difficult to get the closed-form expressions of the coefficients in the analytical solution (Eq. (5)), we use the fixed arc-length continuation method [38] to get numerical values of the coefficients, of the analytical solution, at different values of the excitation frequency for a given value of excitation amplitude. While for the numerical simulations, we have used MATLAB's numerical ode solver "ode45" with high relative and absolute tolerance values. To get the amplitude–frequency response numerically, we uniformly divide the nondimensional excitation frequency, Ω, in a given range. For each value of Ω, numerical simulations are run for a sufficient time to get rid of the system's transient response. Thereafter, the peaks of the time response y_a are plotted for each value of Ω. The comparison between both approaches has been shown in Fig. 2. From Fig. 2, we observe that the response of the system using the analytical approach, HBM, excellently matches with the response of the system using the numerical approach. Having shown that the steady-state responses of the system can be approximated using HBM, we will use the analytical solution (Eq. (5)) in the remainder of the analysis unless otherwise stated.

4.2 Linear Stability Curves. To perform the linear stability analysis of the current system, the complete set of linear ordinary differential equations (ODE's) from Eq. (8) can be written in a compact form as

$$\dot{\mathbf{x}}(\tau) = \mathbf{F}(\tau)\mathbf{x}(\tau)$$

where $\mathbf{F}(\tau)$ is a Jacobian matrix with time-periodic coefficients (due to the appearance of periodic steady-states) and $\mathbf{x}(\tau)$ is a state vector with components $\mathbf{x}(\tau) = [y_1, y_2, y_3, y_4, y_5, y_6]^T$.

To study the stability characteristics of the coupled system, we use the Floquet theory. To generate the stability plot in $F - \Omega$ space, we divide the given range of F and Ω in 1000×500 subregions with 1000 discrete points along the F-axis and 500 discrete points along the Ω-axis. Next, we run the simulation to generate the fundamental matrix and obtain the Floquet multipliers, $f_i s$, as the eigenvalues of the fundamental matrix. For each point, we check the magnitude of the dominant Floquet multiplier. If the magnitude of the dominant Floquet multiplier is less than one, then the system is stable, and if it is greater than one, it becomes unstable. Therefore, the stability boundary is defined as the locus of operating points corresponding to the dominant Floquet

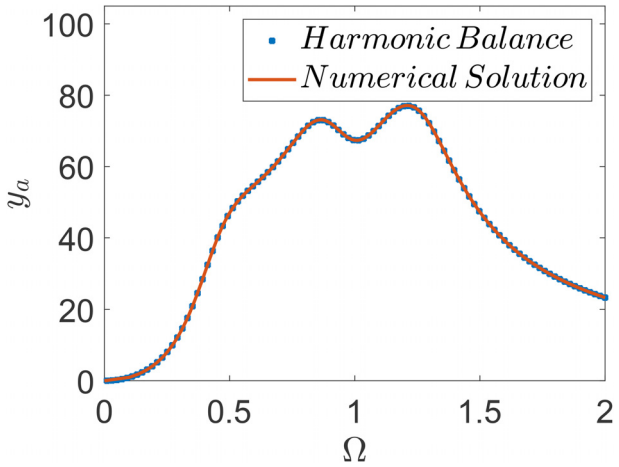

Fig. 2 Comparison of analytical and numerical solutions for $F = 100$ and parameter values listed in Table 1

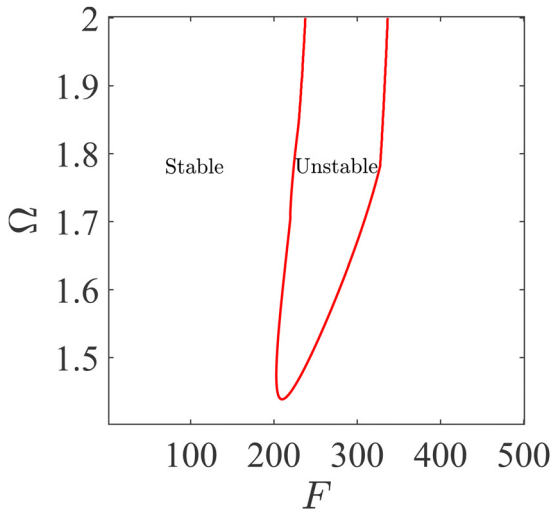

Fig. 3 Stability curve in F–Ω space for the parameter values listed in Table 1

multiplier with magnitude one. After evaluating the dominant Floquet multiplier at every point, the boundary, separating the stable and unstable region is plotted and shown in Fig. 3. From Fig. 3, we observe the transitions in the stability of the periodic steady-states after certain threshold frequencies. To understand the dynamics involved with these transitions, bifurcation diagrams, and Lyapunov spectra are generated and discussed in Sec. 4.3.

4.3 Bifurcation Analysis. For the numerical bifurcation analysis, we have used MATLAB's ODE solver "ode45" with high values of relative and absolute tolerances, " 10^{-8}," to solve our first-order system of ODE's. These bifurcation diagrams can be plotted by fixing either of the control parameters, i.e., F or Ω, and varying the other. In this work, we fix $\Omega(\Omega = 1.6903)$, and vary F in forward/increasing and backward/decreasing directions. To perform the above-mentioned step, we uniformly divide the bifurcation parameter, F, in a given range and run the numerical simulations for a sufficient time to capture the steady-state response of the system at each value of F in both directions. Note that for both forward and backward sweeps, the system's final response for a previous bifurcation parameter is used as the initial condition for the numerical simulation corresponding to the next value of the bifurcation parameter. These bifurcation diagrams, showing the extrema of the hand-arm system's motion, i.e., y_5 (corresponding to $y_6 = 0$) are depicted in Figs. 4 and 5 for relatively low and high values of F, respectively.

Figure 4 shows the bifurcation diagram for $F : 0 - 500$ in forward and backward direction. From Fig. 4, we can observe that the system loses and regains Lyapunov stability. The Lyapunov

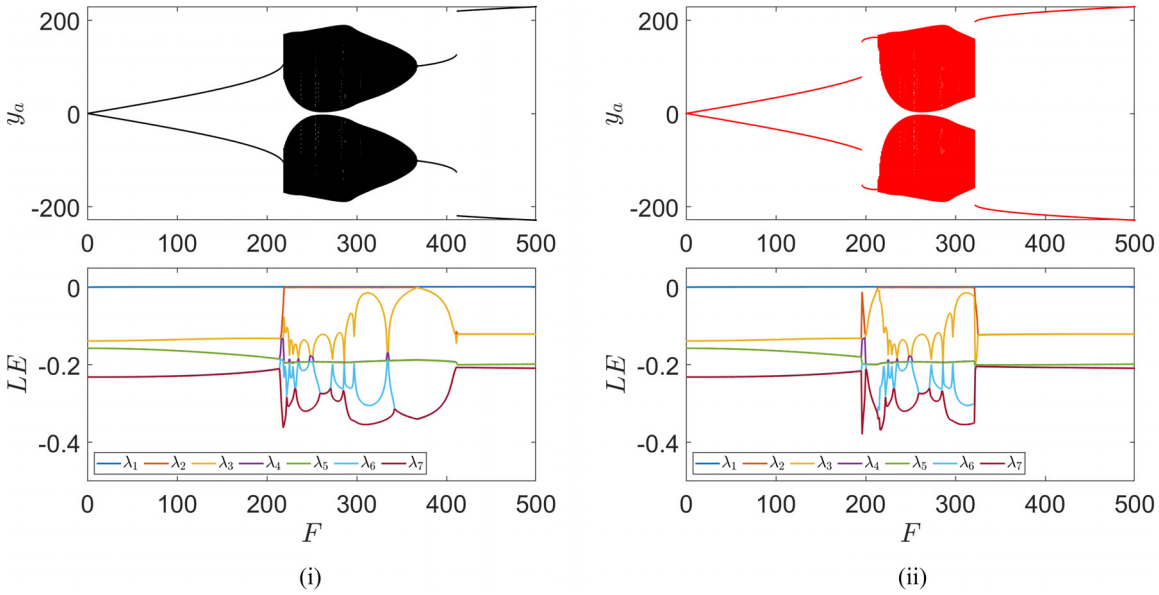

Fig. 4 Bifurcation diagram and its corresponding Lyapunov exponent spectrum for (*i*) forward sweep and (*ii*) backward sweep with $\Omega = 1.6903$ and parameter values listed in Table 1

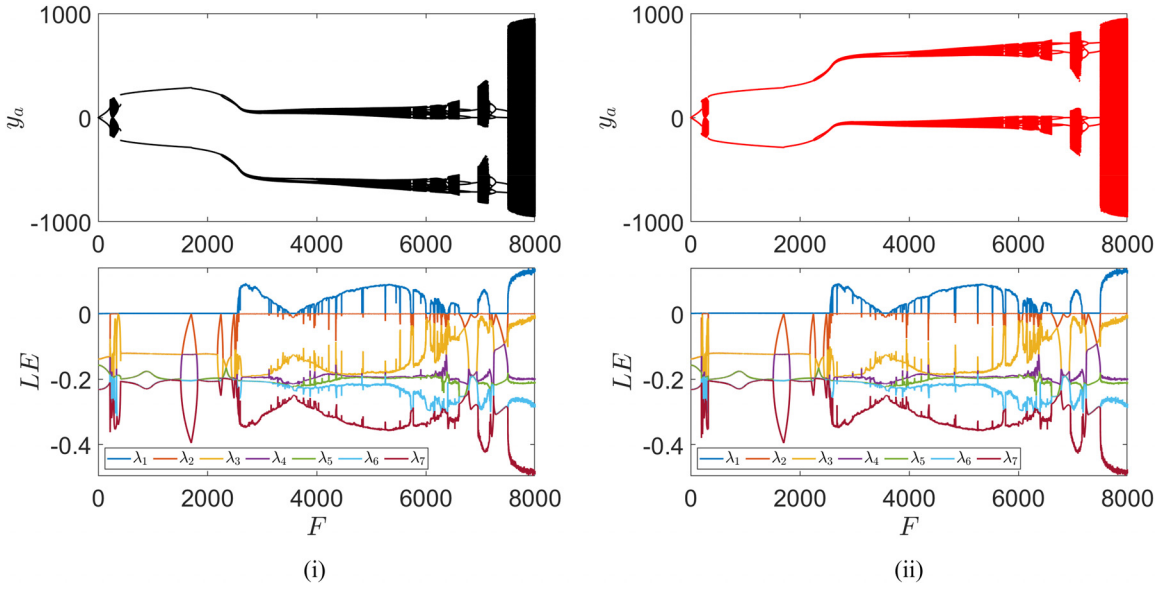

Fig. 5 Bifurcation diagram and its corresponding Lyapunov exponent spectrum for (*i*) forward sweep and (*ii*) backward sweep with Ω set to 1.6903

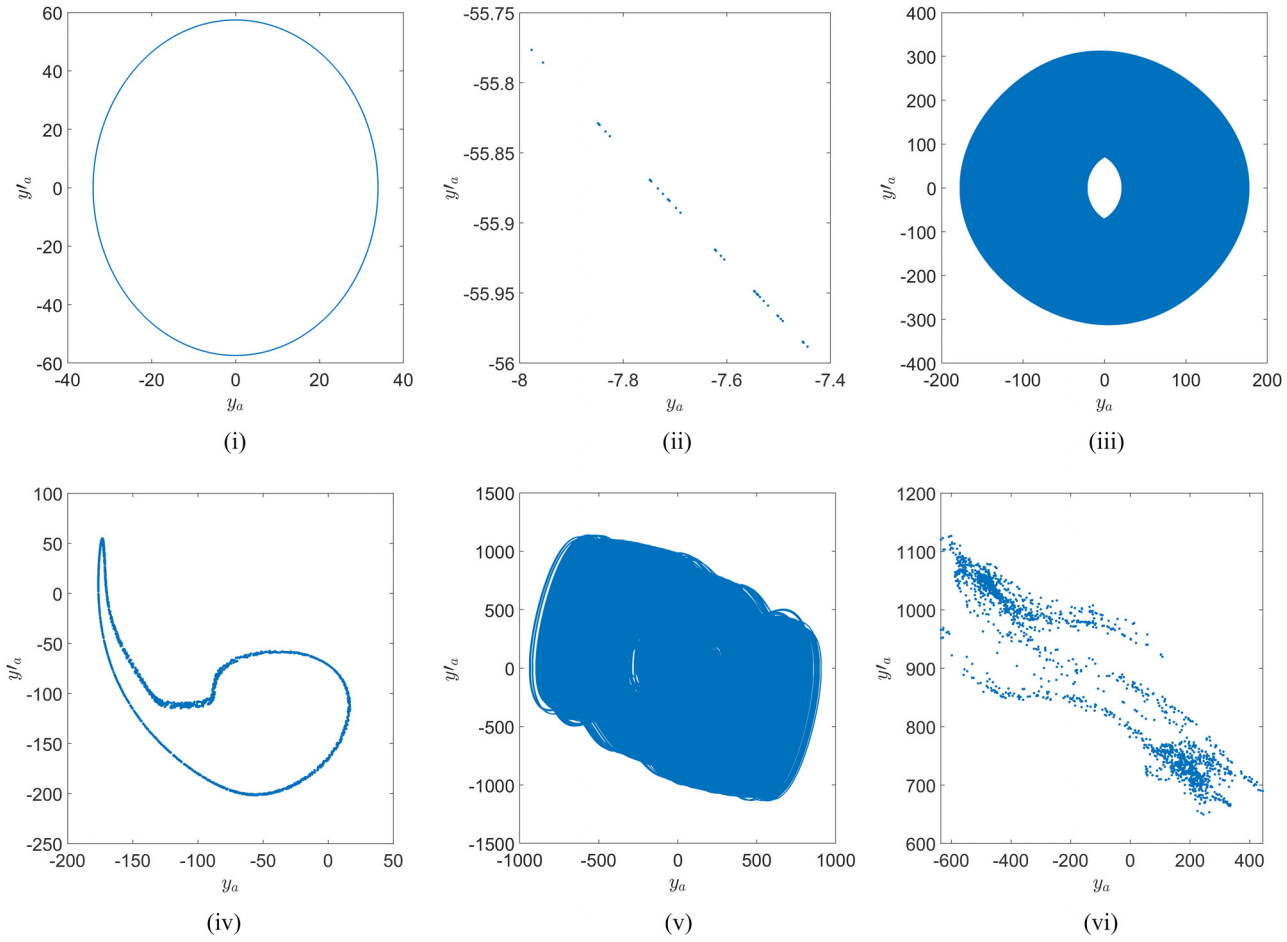

Fig. 6 Phase portraits for (*i*) periodic ($F = 100$), (*iii*) quasi-periodic ($F = 300$), and (*v*) chaotic motion ($F = 7900$), and their corresponding Poincare maps for (*ii*) periodic, (*iv*) quasi-periodic, and (*vi*) chaotic motion for Ω set to 1.6903 are shown. These dynamics correspond to the dynamics obtained via a forward sweep.

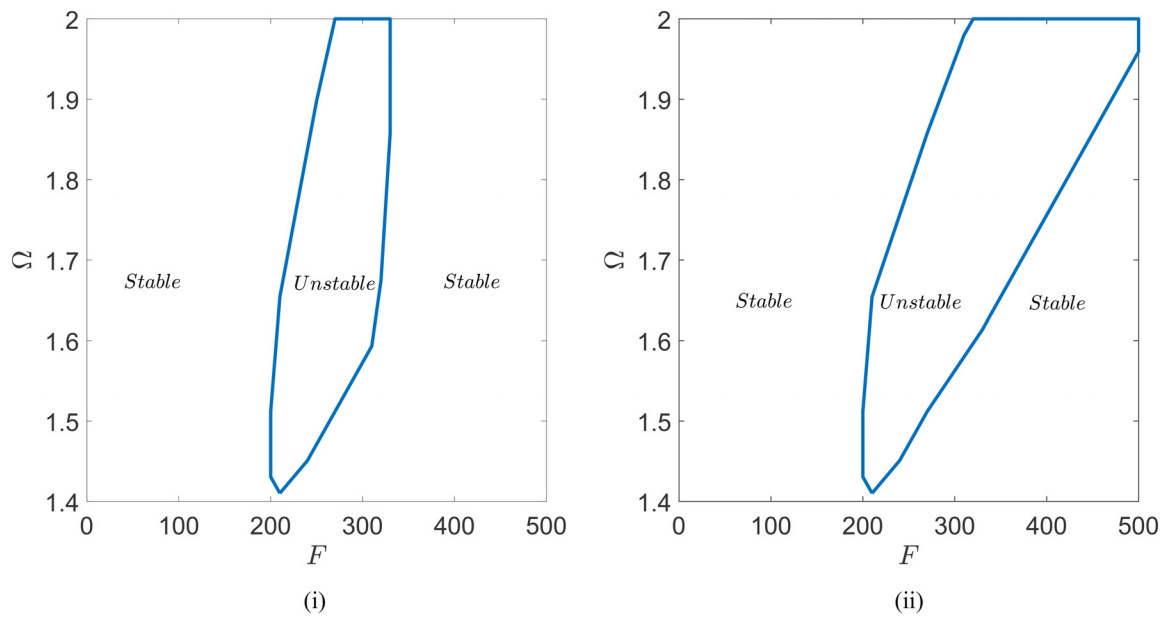

Fig. 7 Lyapunov chart used to highlight different regimes of motion of the system in the parametric space Ω-F obtained via (*i*) a backward sweep and (*ii*) a forward sweep

stable region is also asymptotically stable as predicted by the stability plots (Fig. 3). We further observe the appearance of quasi-periodic motions in the unstable region. The appearance of these quasi-periodic motions can be further confirmed by plotting the variation of Lyapunov exponents. The Lyapunov exponents (LE) of the system are obtained using the method proposed by Wolf et al. [39]. The Lyapunov exponents for this system are obtained with the equations of motion transformed to an autonomous form.

The regions of F for which the largest LE is zero and the other LE's are negative correspond to periodic solutions. While the values of F where the two largest LEs are zero and the other LEs are negative corresponds to quasi-periodic solutions [40,41]. From the Lyapunov spectrum shown in Fig. 4, we can observe that the two largest Lyapunov exponents become zero in the unstable regions, signifying the existence of the quasi-periodic solutions. This observation further verifies our bifurcation and linear stability analyses.

Having established the existence of quasi-periodic solutions in the unstable region, next, we present systems' dynamics for larger values of excitation amplitude $(F)\Omega = 1.6903$, and is shown in Fig. 5 for forward and backward sweeps. This step is performed to explore the dynamics resulting from a change in the stability of the steady periodic solution. From Fig. 5, we can observe that the steady periodic solutions lose stability at higher values of F through quasi-periodic solutions, as two of the dominant Lyapunov exponent become zero. Furthermore, chaotic attractors begin to appear in the system when the quasi-periodic solutions lose their stability. The existence of a chaotic attractor can be further confirmed by the Lyapunov exponent, as the dominant Lyapunov exponent becomes greater than zero. To further confirm the appearance of periodic, quasi-periodic, and chaotic solutions, as indicated by the numerical bifurcation diagrams and Lyapunov exponents, phase portraits, and Poincare sections are generated and are shown in Fig. 6. From Fig. 6, the appearance of periodic motion is confirmed through a closed circular curve on the phase

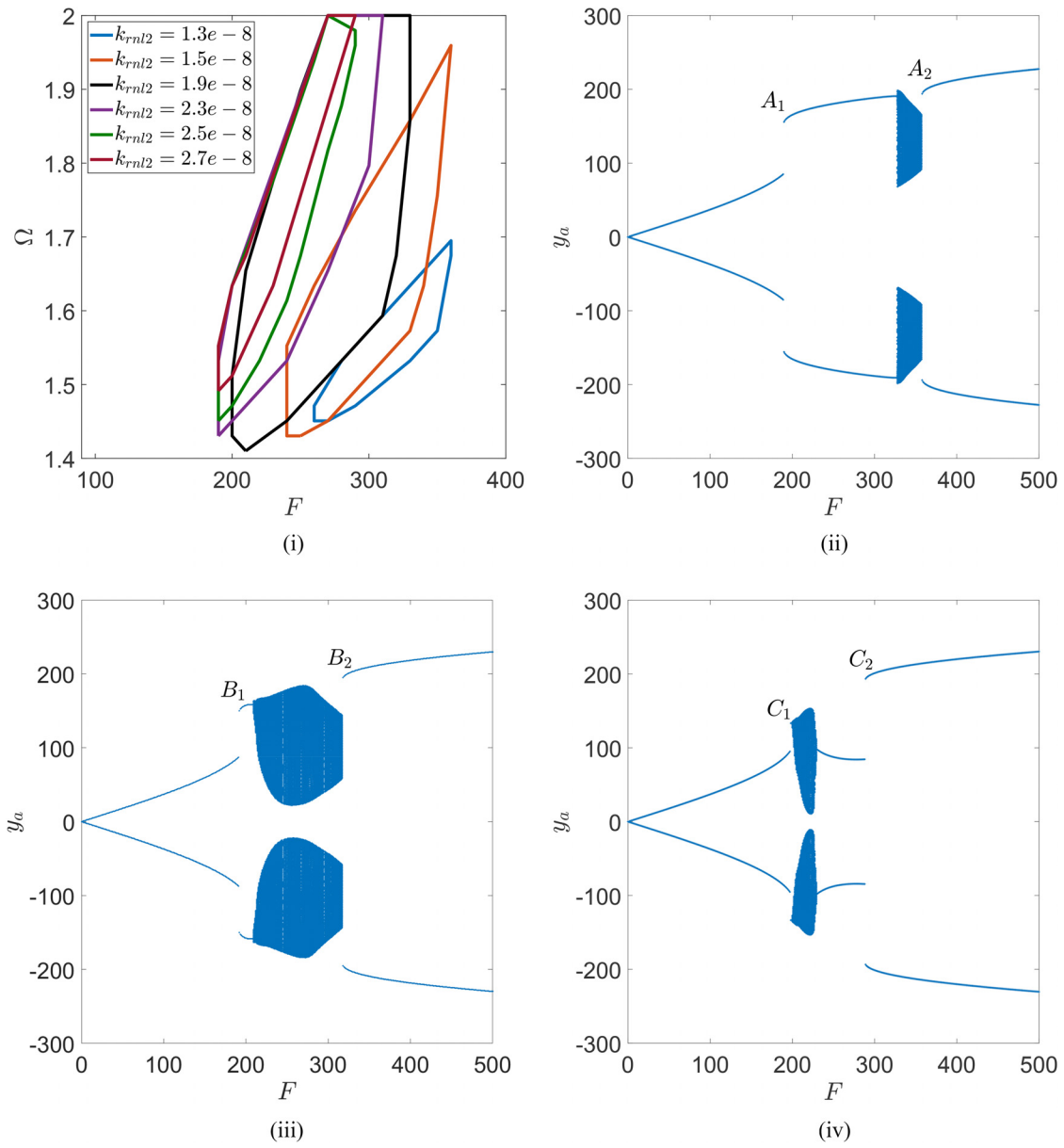

Fig. 8 (*i*) Comparison of Lyapunov chart for different values of k_{rnl2}. Bifurcation diagrams for $\Omega = 1.64$ and $k_{rnl2} =$ (*ii*) 1.3×10^{-8}, (*iii*) 1.9×10^{-8}, and (*iv*) 2.7×10^{-8}. The values of the *x*-coordinates of A_1, A_2, B_1, B_2, C_1, and C_2 are 189, 358, 192, 318, 198, and 289, respectively.

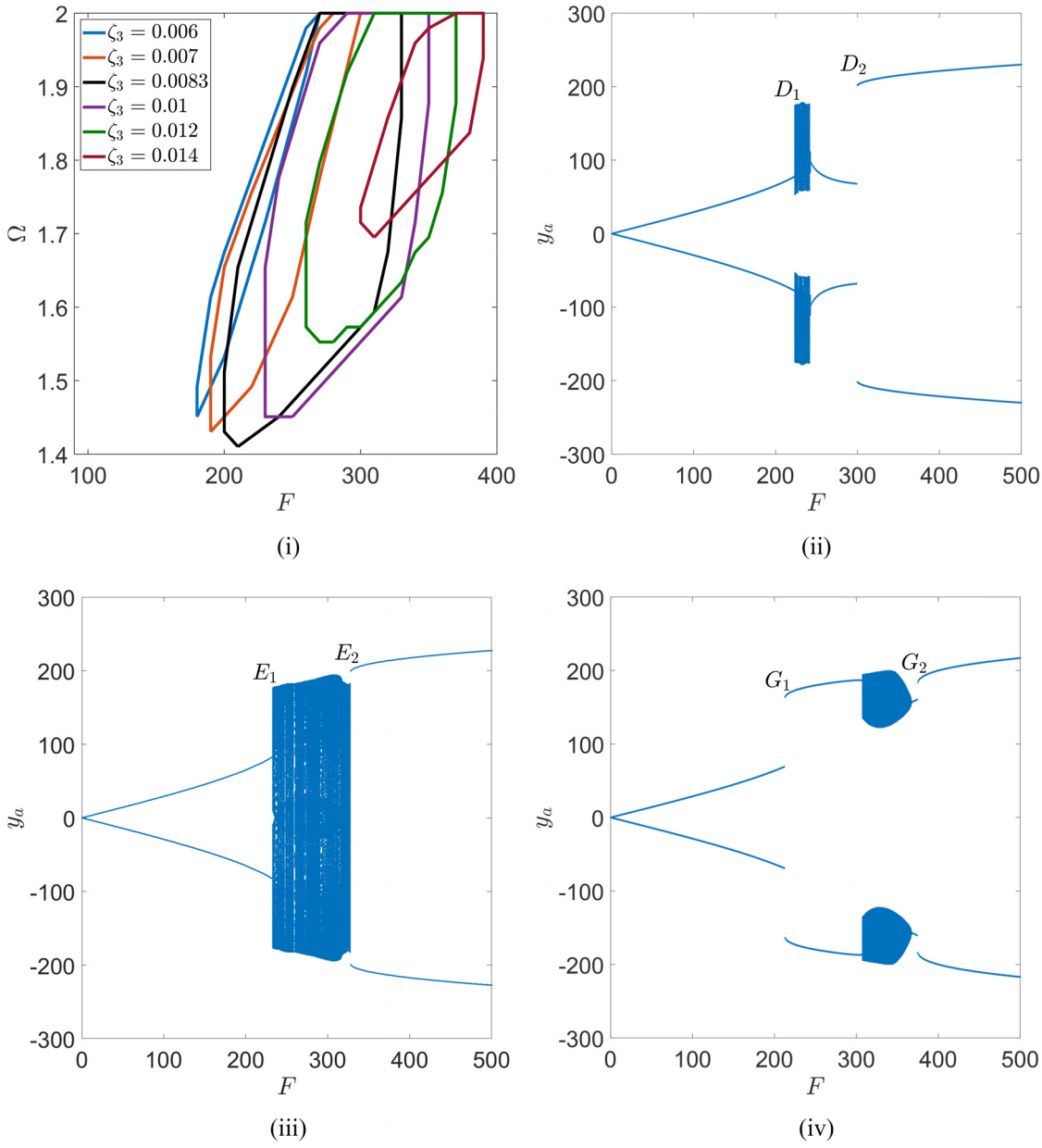

Fig. 9 (*i*) Comparison of Lyapunov chart for different values of ζ_3. Bifurcation diagrams for $\Omega = 1.8$ and $\zeta_3 =$ (*ii*) 0.006, (*iii*) 0.0083, and (*iv*) 0.014. The values of the *x*-coordinates of D_1, D_2, E_1, E_2, G_1, and G_2 are 224, 300, 233, 328, 213, and 375, respectively.

portrait and a set of points on the Poincare section. Also, quasi-periodic and chaotic motions are correctly depicted as a closed curve and a scattered group of points on the Poincare section, respectively. Phase portraits aptly describe quasi-periodic and chaotic motion as dense attractors; however, the Poincare section provides a map that shows a clearer distinction between chaotic and quasi-periodic motions. Next, we explore the effects of different absorber parameters on the performance of the system.

5 Parametric Analysis

In this section, we examine the effects of the absorber parameters on the safe operating region in the parametric space of $F - \Omega$ to avoid the appearance of quasi-periodic and chaotic motion in the coupled HIM-HAS-NVAI system.

Note that if the HAS was modeled as a continuous system, it would consist of multiple natural frequency components. Therefore, when the system is in operation, it would be unsatisfactory if one of the natural frequency components of the HAS matches with one of the frequency components of quasi-periodic or chaotic motion exhibited by the system. Such occurrences could lead to resonance and increase the risk of injury to the HAS. Based on bifurcation diagrams and Lyapunov spectra for the system (Figs. 4 and 5), it has been observed that it is indeed possible for the system to exhibit quasi-periodic and chaotic motion and hence, the possibility of resonance. Therefore, it is desirable to select the absorber parameters such that the appearances of quasi-periodic or chaotic motion can be avoided.

Since Floquet multipliers only provide information about the stability of steady-state periodic solutions of the system, we use the Lyapunov exponents to characterize the systems' behavior in the parametric space of $F - \Omega$. This further helps us to determine safe (only periodic solutions) and unsafe (quasi-periodic and chaotic attractors) regions in the parametric space. As mentioned earlier, for periodic motions, the largest LE is zero, and the other LEs are negative, and for quasi-periodic motions, the two largest LEs

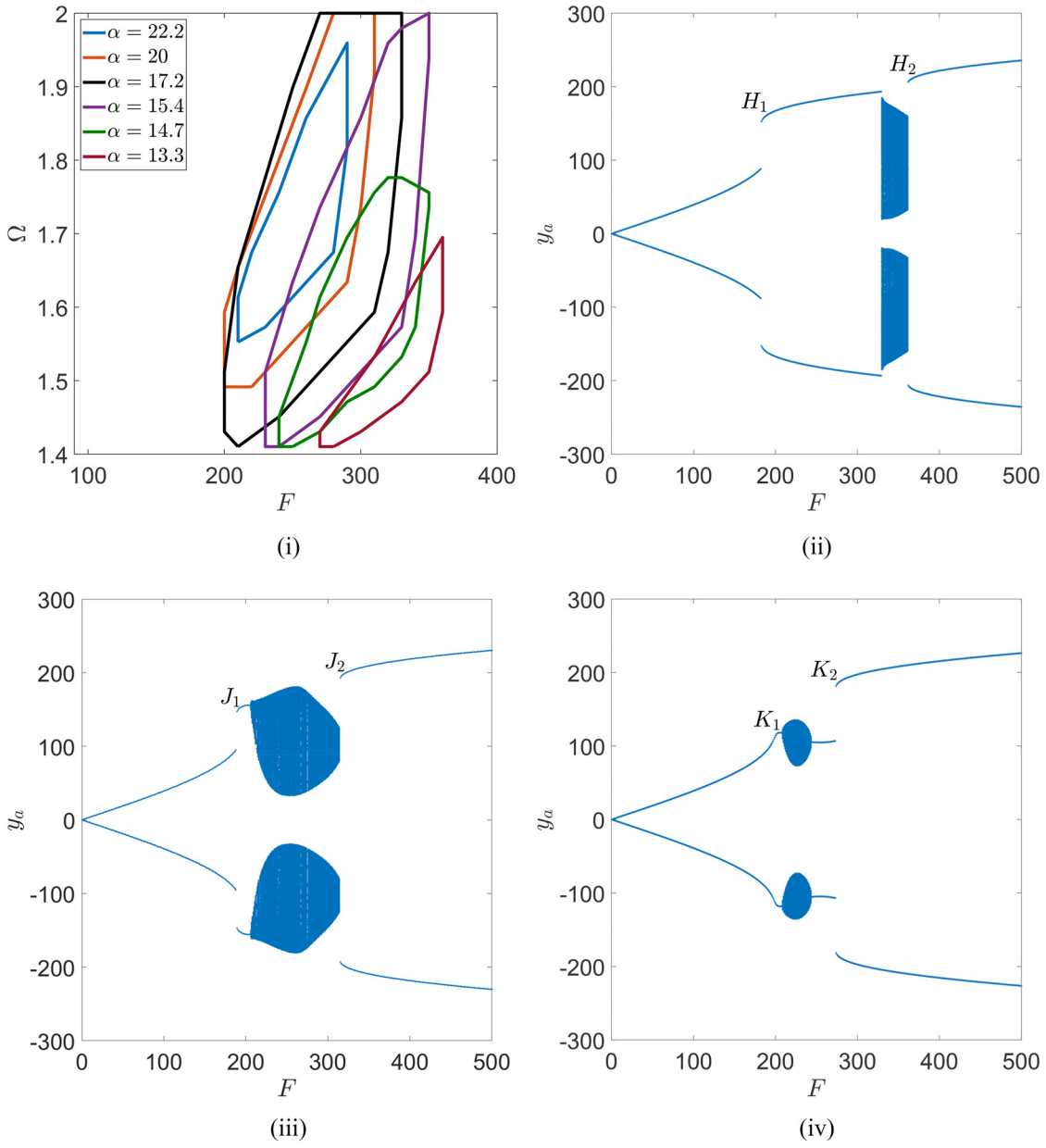

Fig. 10 (*i*) Comparison of Lyapunov chart for different values of α. Bifurcation diagrams for $\Omega = 1.6$ and $\alpha =$ (*ii*) 13.3, (*iii*) 17.5, and (*iv*) 22.2. The values of the *x*-coordinates of H_1, H_2, J_1, J_2, K_1, and K_2 are 183, 362, 189, 315, 209, and 274, respectively.

are zero, and the other LEs are negative. Whereas, for chaotic motions, the leading Lyapunov exponent is positive. Therefore, the boundary separating the safe and unsafe region corresponds to the set of parameters for which the condition for periodic motion is not satisfied. This parametric space within which the system's safe and unsafe operating region is identified will be referred to as a Lyapunov chart.

From Figs. 5(*i*) and 5(*ii*), we observe that for the forward and backward sweeps, both the Lyapunov spectra and bifurcation diagrams detect different ranges of F for the onsets of quasi-periodic and chaotic motions. Therefore, to determine the safe operating region in the parametric space of $F - \Omega$, the Lyapunov chart is obtained by both forward and backward sweeps for the system parameter values listed in Table 1. To obtain the Lyapunov charts in both forward and backward sweeps, we divide the parametric space into 60 discrete points along the Ω-axis and 50 discrete points along the F-axis. For each value of Ω between 1.4 and 2, the Lyapunov exponents are obtained for different values of F between 0 and 500 in both forward and backward sweeps. Finally, with the use of these Lyapunov exponents, we obtain the boundary between the safe and unsafe operating region of the system.

Based on Figs. 7(*i*) and 7(*ii*), we can observe that the Lyapunov chart in backward sweep detects the onset of chaotic or quasi-periodic motion earlier (with regards to F) than the Lyapunov chart obtained by forward sweep. In this study, we would like to detect the early onset of the unsafe operation region of the system. Therefore, the Lyapunov chart obtained by a backward sweep will be used for further analysis. Next, the effect of different absorber parameters on the system's performance is characterized using the Lyapunov chart.

The effect of k_{rnl2} on the performance of the absorber is shown in Fig. 8. From this figure, we observe that the area of the unsafe operating region increases with an increase in k_{rnl2} till the value of $k_{rnl2} = 1.9 \times 10^{-8}$. When k_{rnl2} is increased past 1.9×10^{-8}, the area of the unsafe operating region starts decreasing. This observation implies that for given system parameters, there is a critical value of k_{rnl2}, which maximizes the unsafe operating region.

In this work, we set two criteria for an efficient design of the NVAI: delay of the onset of the unsafe operating region as the primary criterion and minimization of the area of the unsafe operating region as the secondary criterion. From Fig. 8, we can observe that smaller values of k_{rnl2} satisfy the criteria set, and hence can be selected for an efficient absorber design.

Next, a quantitative examination of the effect of varying values of k_{rnl2} on the system's dynamics is shown through bifurcation diagrams (Fig. 8). From Figs. 8(*ii*)–8(*iv*), we can observe that the value of F (x-coordinate) corresponds to the first instance of a significant jump in the amplitude of a periodic solution (A_1, B_1, and C_1) increases with increase in k_{rnl2}. Furthermore, the point corresponding to the second jump to higher amplitude periodic motion from quasi-periodic or periodic oscillations (A_2, B_2, and C_2) decreases with increase in k_{rnl2}. Further, the value of F corresponding to the onset of quasi-periodic motion begins to move toward the first location of the sudden jump in the amplitude of periodic solutions as k_{rnl2} increases. This further implies the early onset of the unsafe operating region as the k_{rnl2} increases.

Next, the effect of ζ_3 on the performance of the absorber is shown in Fig. 9. From Fig. 9, we can observe that the area of the unsafe operating region of the system increases with an increase in ζ_3 up to $\zeta_3 = 0.0083$. After this value of ζ_3, the area of the unsafe operating region starts decreasing. This further implies that for the system parameter values listed in Table 1, the critical value of ζ_3 is 0.008, which maximizes the unsafe operating region. Also, as ζ_3 increases, the value of F corresponding to the onset of unsafe operating region increases. This observation further implies that the larger values of the absorber nondimensional damping, ζ_3, satisfy the subjective criteria defined earlier for an efficient absorber design.

Similar to the case of k_{rnl2}, bifurcation diagrams are used to assess the quantitative effect of varying values of ζ_3 on the performance of the system. Based on Figs. 9(*ii*)–9(*iv*), we can observe that an increase in value of ζ_3 results in an increase in the distance between the values of F corresponding to the first (D_1, E_1, G_1) and second instance (D_2, E_2, G_2) of the sudden jump in the response of the system. Furthermore, the higher value of ζ_3 delays the onset of the quasi-periodic motions and hence, satisfies the design criteria for an efficient absorber.

Finally, the role of α on the performance of the system is presented in Fig. 10. The results show that decreasing values of α from 22.2 to 17.2 causes an increase in the area of the unsafe operating region of the system. However, when the value of α is decreased past 17.2, the size of the unsafe operating region of the system starts decreasing. Also, as the value of α decreases, the values of F spanned by the unsafe operating region increase. Thus, it can be seen that the smaller values of the α satisfy the subjective criteria defined earlier for having an efficient absorber design. Similar to the previous parametric studies, we now explore the effects of varying α on the system's performance using bifurcation diagrams. As α is increased from 13.3 to 14.7, the distance between the F values for the first and second location where there is a jump to higher amplitude motion decreases. Then at $\alpha = 22.2$, only one location now exists where there is a significant jump to high amplitude motion, i.e., at K_2.

The results of this parametric study imply that the absorber properties related to the above studied nondimensional parameters, i.e., the absorber's stiffness, damping, and inertance, can be appropriately tuned to increase the safe operating region in the parametric space of $F - \Omega$. Also, as revealed by the bifurcation diagrams, the absorber parameters can be appropriately selected to delay or hasten the onset of a jump in the amplitude of the system's motion when F is used as a bifurcation parameter.

6 Conclusion

In this study, a nonlinear absorber's ability to eliminate or reduce harmful transmission of vibrations from an HIM to the HAS was explored. The method of harmonic balance was used to get an analytical solution for the system. A linear stability analysis, which uses the analytical solution, was performed using the Floquet theory. The system's linear stability analysis revealed unstable and stable regions in the parametric space of excitation amplitude versus excitation frequency ($F - \Omega$). Further exploration of the stable and unstable regions using bifurcation diagrams and a Lyapunov spectrum revealed periodic motion in the stable region and quasi-periodic motion in the unstable space. For a broader range of forcing amplitude parameters, i.e., for $F : 0 - 8000$, bifurcation diagrams, Lyapunov exponents, Phase portraits, and Poincare maps revealed the existence of chaotic solutions. These results also confirmed that Poincare maps better distinguish between quasi-periodic and chaotic motions than phase portraits.

Further, Lyapunov exponents were used to identify quasi-periodic and chaotic motion regions, also referred to as unsafe operating regions, in the excitation force amplitude–frequency ($F - \Omega$) parametric space. Subsequently, a parametric study was performed to observe the effect of varying the absorber's parameters, k_{rnl2}, ζ_3, and α, on the area of the unsafe operating region of the system and on the delay of the onset of the unsafe operating region. This parametric study revealed that the largest value of the nondimensional parameter ζ_3, and the smallest value of α and k_{rnl2} meet the criteria for having the best absorber design parameters. A parametric study using bifurcation diagrams, with bifurcation parameter F, also revealed that a change in k_{rnl2}, ζ_3, and α could control the points at which a sudden jump in the nondimensional amplitude related to the displacement of the HAS occurs.

Data Availability Statement

The datasets generated during and/or analyzed during this study are available from the corresponding author upon reasonable request.

Conflict of Interest

The authors declare that they have no conflict of interest.

Appendix: Expressions Used in Eqs. (1), (3), and (6)

$$[\mathbf{M}] = \begin{bmatrix} m_H + m_s & 0 & 0 \\ 0 & m_a & 0 \\ 0 & 0 & m_N + b \end{bmatrix}$$

$$[\mathbf{C}] = \begin{bmatrix} c_H + c_N + c_s & -c_s & -c_N \\ -c_s & c_a + c_s & 0 \\ -c_N & 0 & c_N \end{bmatrix}$$

$$[\mathbf{K}] = \begin{bmatrix} k_{HL} + k_{NL} + k_s & -k_s & -k_{NL} \\ -k_s & k_a + k_s & 0 \\ -k_{NL} & 0 & k_{NL} \end{bmatrix}$$

$$[\mathbf{f}_{nl}] = \begin{bmatrix} k_N(x_H - x_N)^3 + k_H x_H^3 \\ 0 \\ k_N(x_N - x_H)^3 \end{bmatrix}$$

$$[\mathbf{F}_{eq}] = \begin{bmatrix} F_w \\ 0 \\ 0 \end{bmatrix}$$

$$[\mathbf{M1}] = \begin{bmatrix} 1 & 0 & 0 \\ 0 & 1 & 0 \\ 0 & 0 & 1 \end{bmatrix}$$

$$[\mathbf{C1}] = \begin{bmatrix} -2\zeta_1 + 2\zeta_2 + 2\zeta_3 & -2\zeta_2 & -2\zeta_3 \\ -2\zeta_3\alpha & 0 & 2\zeta_3\alpha \\ -2\zeta_2\alpha_2 & 2\zeta_4\alpha_2 + 2\zeta_2\alpha_2 & 0 \end{bmatrix}$$

$$[\mathbf{K1}] = \begin{bmatrix} 1+k_{r1}+k_{r2} & -k_{r1} & -k_{r2} \\ -k_{r2}\alpha & 0 & k_{r2}\alpha \\ -k_{r1}\alpha_2 & k_{r3}\alpha_2 + k_{r1}\alpha_2 & 0 \end{bmatrix}$$

$$[\mathbf{f}_{nl}] = \begin{bmatrix} k_{rnl1}y_H^3 + k_{rnl2}(y_H - y_N)^3 \\ k_{rnl2}\alpha(y_N - y_H)^3 \\ 0 \end{bmatrix}$$

$$[\mathbf{F1}_{eq}] = \begin{bmatrix} F\Omega^2\sin(\Omega\tau) \\ 0 \\ 0 \end{bmatrix}$$

$$[\mathbf{A}] = \begin{bmatrix} 0 & -1 & 0 & 0 & 0 & 0 \\ k_{r1}+k_{r2}+1 & -2\zeta_1+2\zeta_2+2\zeta_3 & -k_{r1} & -2\zeta_2 & -k_{r2} & -2\zeta_3 \\ 0 & 0 & 0 & -1 & 0 & 0 \\ \alpha(-k_{r2}) & -2\alpha\zeta_3 & 0 & 0 & \alpha k_{r2} & 2\alpha\zeta_3 \\ 0 & 0 & 0 & 0 & 0 & -1 \\ \alpha_2(-k_{r1}) & -2\alpha_2\zeta_2 & \alpha_2 k_{r1}+\alpha_2 k_{r3} & 2\alpha_2\zeta_2+2\alpha_2\zeta_4 & 0 & 0 \end{bmatrix}$$

$$[\mathbf{N}_1] = \begin{bmatrix} 0 \\ k_{\mathrm{nl1}}(C_1\cos(\Omega\tau)+D_1\sin(\Omega\tau))^3 + k_{\mathrm{n2}}\left((C_1-C_5)\cos(\Omega\tau)+(D_1-D_5)\sin(\Omega\tau)\right)^3 \\ 0 \\ \alpha k_{\mathrm{nl}22}\Big((C_1\cos(\Omega\tau)+D_1\sin(\Omega\tau))^3 + 3(C_5\cos(\Omega\tau)+D_5\sin(\Omega\tau))(C_1\cos(\Omega\tau)+D_1\sin(\Omega\tau))^2 - 3(C_5\cos(\Omega\tau)+D_5\sin(\Omega\tau))^2(C_1\cos(\Omega\tau)+D_1\sin(\Omega\tau)) + (C_5\cos(\Omega\tau)+D_5\sin(\Omega\tau))^3\Big) \\ 0 \\ 0 \end{bmatrix}$$

$$[\mathbf{F}_{\mathrm{eq}}] = \begin{bmatrix} 0 \\ F\Omega^2\sin(\Omega\tau) \\ 0 \\ 0 \\ 0 \\ 0 \end{bmatrix}$$

References

[1] Griffin, M. J., 2012, *Handbook of Human Vibration*, Academic Press, Cambridge, MA.

[2] Bernard, B. P., and Putz-Anderson, V., 1997, "Musculoskeletal Disorders and Workplace Factors; a Critical Review of Epidemiologic Evidence for Work-Related Musculoskeletal Disorders of the Neck, Upper Extremity, and Low Back,".

[3] ISO, 2001, *Mechanical Vibration-Measurement and Evaluation of Human Exposure to Handtransmitted Vibration - Part 1: General Requirements*, International Organization for Standardization, Geneva, Switzerland, Standard No. ISO 5349–1.

[4] Vihlborg, P., Bryngelsson, L., Lindgren, B., Gunnar Gunnarsson, L., and Graff, P., 2017, "Association Between Vibration Exposure and Hand-Arm Vibration Symptoms in a Swedish Mechanical Industry," Int. J. Ind. Ergonom., **62**, pp. 77–81.

[5] Dong, R. G., Welcome, D. E., Xu, X., Chen, Q., Lin, H., McDowell, T. W., and Wu, J. Z., 2018, "A Model for Simulating Vibration Responses of Grinding Machine-Workpiece-Hand-Arm Systems," J. Sound Vib., **431**, pp. 276–294.

[6] Wu, S.-T., and Shao, Y.-J., 2007, "Adaptive Vibration Control Using a Virtual-Vibration-Absorber Controller," J. Sound Vib., **305**(4–5), pp. 891–903.

[7] Sims, N. D., 2007, "Vibration Absorbers for Chatter Suppression: A New Analytical Tuning Methodology," J. Sound Vib., **301**(3–5), pp. 592–607.

[8] Jang, S.-J., Brennan, M. J., Rustighi, E., and Jung, H.-J., 2012, "A Simple Method for Choosing the Parameters of a Two Degree-of-Freedom Tuned Vibration Absorber," J. Sound Vib., **331**(21), pp. 4658–4667.

[9] Frahm, H., April 18 1911, "Device for Damping Vibrations of Bodies," US Patent No. 989,958.

[10] Hao, K. Y., and Ripin, Z. M., 2013, "Nodal Control of Grass Trimmer Handle Vibration," Int. J. Ind. Ergonom., **43**(1), pp. 18–30.

[11] Liu, W. B., Dai, H. L., and Wang, L., 2017, "Suppressing Wind-Induced Oscillations of Prismatic Structures by Dynamic Vibration Absorbers," Int. J. Struct. Stabil. Dyn., **17**(6), p. 1750056.

[12] Barry, O., and Bukhari, M., 2017, "On the Modeling and Analysis of an Energy Harvester Moving Vibration Absorber for Power Lines," ASME Paper No. DSCC2017-5377.

[13] Febbo, M., 2012, "Optimal Parameters and Characteristics of a Three Degree of Freedom Dynamic Vibration Absorber. Journal of Vibration and Acoustics," ASME J. Vib. Acoust., **134**(2), p. 021010.

[14] Shakeri, S., and Samani, F. S., 2017, "Application of Linear and nonlinear vibration absorbers in Micromilling Process in Order to Suppress Regenerative Chatter," Nonlinear Dyn., **89**(2), pp. 851–862.

[15] Moradi, H., Bakhtiari-Nejad, F., and Movahhedy, M. R., 2008, "Tuneable Vibration Absorber Design to Suppress Vibrations: An Application in Boring Manufacturing Process," J. Sound Vib., **318**(12), pp. 93–108.

[16] Carpineto, N., Lacarbonara, W., and Vestroni, F., 2014, "Hysteretic Tuned Mass Dampers for Structural Vibration Mitigation," J. Sound Vib., **333**(5), pp. 1302–1318.

[17] Poovarodom, N., Kanchanosot, S., and Warnitchai, P., 2003, "Application of Non-Linear Multiple Tuned Mass Dampers to Suppress Man-Induced Vibrations of a Pedestrian Bridge," Earthquake Eng. Struct. Dyn., **32**(7), pp.1117–1131.

[18] Lacarbonara, W., and Cetraro, M., 2011, "Flutter Control of a Lifting Surface Via Visco-Hysteretic Vibration Absorbers," Int. J. Aeronaut. Space Sci., **12**(4), pp. 331–345.

[19] Wang, M., 2011, "Feasibility Study of Nonlinear Tuned Mass Damper for Machining Chatter Suppression," J. Sound Vib., **330**(9), pp.1917–1930.

[20] Lindell, H., Berbyuk, V., Josefsson, M., and Leó Grétarsson, S., 2015, "Nonlinear Dynamic Absorber to Reduce Vibration in Hand-Held Impact Machines," Proceedings of the International Conference on Engineering Vibration, Ljubljana, Sept. 7–10, pp. 1530–1539.

[21] Viguié, R., and Kerschen, G., 2009, "Nonlinear Vibration Absorber Coupled to a Nonlinear Primary System: A Tuning Methodology," J. Sound Vib., **326**(3–5), pp. 780–793.

[22] Habib, G., Detroux, T., Viguié, R., and Kerschen, G., 2015, "Nonlinear Generalization of Den Hartog's Equal-Peak Method," Mech. Syst. Signal Process., **52**, pp. 17–28.

[23] Hoang, N., Fujino, Y., and Warnitchai, P., 2008, "Optimal Tuned Mass Damper for Seismic Applications and Practical Design Formulas," Eng. Struct., **30**(3), pp. 707–715.

[24] De Angelis, M., Perno, S., and Reggio, A., 2012, "Dynamic Response and Optimal Design of Structures With Large Mass Ratio TMD," Earthquake Eng. Struct. Dyn., **41**(1), pp. 41–60.

[25] Alabi, O., and Barry, O., 2020, "On the Nonlinear Vibration Analysis of a Hand-Held Impact Machine," ASME Paper No. DSCC2020-3155.

[26] Bae, J.-S., Hwang, J.-H., Roh, J.-H., Kim, J.-H., Yi, M.-S., and Lim, J. H., 2012, "Vibration Suppression of a Cantilever Beam Using Magnetically Tuned-Mass-Damper," J. Sound Vib., **331**(26), pp. 5669–5684.

[27] Joubaneh, E. F., and Barry, O. R., 2019, "On the Improvement of Vibration Mitigation and Energy Harvesting Using Electromagnetic Vibration Absorber-Inerter: Exact h2 Optimization," ASME J. Vib. Acoust., **141**(6), p. 061007.

[28] Ikago, K., Saito, K., and Inoue, N., 2012, "Seismic Control of Single-Degree-of-Freedom Structure Using Tuned Viscous Mass Damper," Earthquake Eng. Struct. Dyn., **41**(3), pp. 453–474.

[29] Golysheva, E. V., Babitsky, V. I., and Veprik, A. M., 2004, "Vibration Protection for an Operator of a Hand-Held Percussion Machine," J. Sound Vib., **274**(1–2), pp. 351–367.
[30] Moon, F. C., and Kalmar-Nagy, T., 2001, "Nonlinear Models for Complex Dynamics in Cutting Materials," Philos. Trans. R. Soc. London. Ser. A Math., Phys. Eng. Sci., **359**(1781), pp. 695–711.
[31] Nayfeh, A. H., 1986, "Perturbation Methods in Nonlinear Dynamics," *Lecture Notes in Physics*, Vol. 247, Springer, Berlin.
[32] Stépán, G., and Kalmár-Nagy, T., 1997, "Nonlinear Regenerative Machine Tool Vibrations," ASME Paper No. DETC97/VIB-4021.
[33] Dong, R. G., Welcome, D. E., Wu, J. Z., and McDowell, T. W., 2008, "Development of Hand-Arm System Models for Vibrating Tool Analysis and Test Rig Construction," Noise Control Eng. J., **56**(1), pp.35–44.
[34] Josefsson, M., and Grétarsson, S. L., 2015, "Optimisation of a Non-Linear Tuned Vibration Absorber in a Hand-Held Impact Machine," Master's thesis, Chalmers Univeristy of Technology, Gothenburg, Sweden.
[35] Krack, M., and Gross, J., 2019, *Harmonic Balance for Nonlinear Vibration Problems*, Vol. 1, Springer, New York.
[36] Asami, T., Nishihara, O., and Baz, A. M., 2002, "Analytical Solutions to h ∞ and h 2 Optimization of Dynamic Vibration Absorbers Attached to Damped Linear Systems," ASME J. Vib. Acoust., **124**(2), pp. 284–295.
[37] Grappasonni, C., Habib, G., Detroux, T., Wang, F., Kerschen, G., and Jensen, J. S., 2014, "Practical Design of a Nonlinear Tuned Vibration Absorber," Proceedings of the ISMA Conference, Leuven, Belgium, Sept. 15–19, pp. 3029–3046.
[38] Wahi, P., 2005, "A Study of Delay Differential Equations with Applications to Machine Tool Vibrations," Ph.D. thesis, Indian Institute of Science, Bangalore, India.
[39] Wolf, A., 1986, "Quantifying Chaos With Lyapunov Exponents," Chaos, A. V. Holden, Princeton University Press, Princeton, NJ, pp. 273–290.
[40] Balcerzak, M., Pikunov, D., and Dabrowski, A., 2018, "The Fastest, Simplified Method of Lyapunov Exponents Spectrum Estimation for Continuous-Time Dynamical Systems," Nonlinear Dyn., **94**(4), pp. 3053–3065.
[41] Parker, T. S., and Chua, L., 2012, *Practical Numerical Algorithms for Chaotic Systems*, Springer Science & Business Media, New York.